

# Ex-vivo quantification of ovine pia arachnoid complex biomechanical properties under uniaxial tension

**Gabryel Conley Natividad**

University of Idaho

**Sophia K Theodossiou**

University of Idaho

**Nathan R Schiele**

University of Idaho

**Gordon K Murdoch**

University of Idaho

**Alkiviadis Tsamis**

University of Leicester

**Bertrand Tanner**

Washington State University

**Gabriel Potirniche**

University of Idaho

**Martin Mortazavi**

California Institute of Neuroscience

**David Vorp**

University of Pittsburgh

**Bryn Martin** (✉ [brynm@uidaho.edu](mailto:brynm@uidaho.edu))

University of Idaho <https://orcid.org/0000-0003-1234-7880>

---

## Research

**Keywords:** pia-arachnoid complex (PAC), biomechanical properties, uniaxial tension, Ex-vivo quantification

**Posted Date:** October 21st, 2020

**DOI:** <https://doi.org/10.21203/rs.3.rs-58849/v2>

**License:**   This work is licensed under a Creative Commons Attribution 4.0 International License.

[Read Full License](#)

---

**Version of Record:** A version of this preprint was published on November 12th, 2020. See the published version at <https://doi.org/10.1186/s12987-020-00229-w>.

1 **Title**  
2 Ex-vivo quantification of ovine pia arachnoid complex biomechanical properties under uniaxial  
3 tension  
4

5 **Journal to be submitted to**  
6 Fluids and Barriers of the CNS  
7 [https://fluidsbarrierscns.biomedcentral.com/submission-guidelines/preparing-your-](https://fluidsbarrierscns.biomedcentral.com/submission-guidelines/preparing-your-manuscript/research)  
8 [manuscript/research](https://fluidsbarrierscns.biomedcentral.com/submission-guidelines/preparing-your-manuscript/research)  
9

10 **Authors**

11 Gabryel Conley Natividad<sup>1</sup>  
12 Email: conl7344@vandals.uidaho.edu  
13 Phone: +001 208 885 1030  
14

15 Sophia K. Theodossiou<sup>1</sup>  
16 Email: theo4146@vandals.uidaho.edu  
17 Phone: +001 208 885 1030  
18

19 Nathan R. Schiele<sup>1</sup>  
20 Email: nrschiele@uidaho.edu  
21 Phone: +001 208 885 9063  
22

23 Gordon K. Murdoch<sup>2</sup>  
24 Email: gmurdoch@uidaho.edu  
25 Phone: +001 208 885 7370  
26

27 Alkiviadis Tsamis<sup>3</sup>  
28 Email: at441@leicester.ac.uk  
29 Phone: +44 (0) 116 252 3716  
30

31 Bertrand Tanner<sup>4</sup>  
32 Email: Bertrand.tanner@wsu.edu  
33 Phone: +001 5\_09 335 7785  
34

35 Gabriel Potirniche<sup>5</sup>  
36 Email: gabrielp@uidaho.edu  
37 Phone: +001 208 885 4049  
38

39 Martin Mortazavi<sup>6</sup>  
40 Email: m\_mortazavi@hotmail.com  
41 Phone: +001 805 795 7656  
42

43 David A. Vorp<sup>7</sup>  
44 Email: Not given  
45 Phone: Not given  
46

47 **Corresponding Author**

48 Bryn A. Martin<sup>1,8</sup>

49 Email: brynm@uidaho.edu

50 Phone: +001 208 885 1030

51 875 Perimeter Dr. M/C 0904

52 University of Idaho,

53 Moscow, Idaho 83844-0904

54

55 **Author Affiliations**

56 <sup>1</sup>Department of Chemical and Biological Engineering, University of Idaho, 875 Perimeter Dr.  
57 MS0904, Moscow, ID, 83844, U.S.A.

58 <sup>2</sup>Department of Animal & Veterinary Science, University of Idaho, 875 Perimeter Dr. MC1122,  
59 Moscow, ID, 83844-2330, U.S.A.

60 <sup>3</sup>School of Engineering, University of Leicester, University Road, Leicester, LE1 7RH, United  
61 Kingdom

62 <sup>4</sup>Department of Integrated Physiology and Neuroscience, Washington State University, 1815  
63 Ferdinand's Lane, Pullman, WA, 99164, U.S.A.

64 <sup>5</sup>Department of Mechanical Engineering, University of Idaho, 875 Perimeter Dr. MC1122,  
65 Moscow, ID, 83844-1122, U.S.A.

66 <sup>6</sup>National Skull Base Foundation, 2100 Lynn Rd #120, Thousand Oaks, CA, 91360, U.S.A.

67 <sup>7</sup>Departments of Bioengineering, Cardiothoracic Surgery, Surgery, and Chemical & Petroleum  
68 Engineering, and the Clinical and Translational Sciences Institute, University of Pittsburgh, 3700  
69 O'Hara Street, Pittsburgh, PA, 15261, U.S.A.

70 <sup>8</sup>Alcyone Therapeutics Inc., Lowell, MA, 01852

71

72 **ABSTRACT**

73 Background: The pia arachnoid complex (PAC) is a cerebrospinal fluid-filled tissue conglomerate  
74 that surrounds the brain and spinal cord. Pia mater adheres directly to the surface of the brain while  
75 the arachnoid mater adheres to the deep surface of the dura mater. Collagen fibers, known as  
76 subarachnoid trabeculae (SAT) fibers, and microvascular structure lie intermediately to the pia and  
77 arachnoid meninges. Due to its structural role, alterations to the biomechanical properties of the  
78 PAC may change surface stress loading in traumatic brain injury (TBI) caused by sub-concussive  
79 hits. The aim of this study was to quantify the mechanical and morphological properties of ovine  
80 PAC.

81 Methods: Ovine brain samples (n=10) were removed from the skull and tissue was harvested  
82 within 30 minutes post-mortem. To access the PAC, ovine skulls were split medially from the  
83 occipital region down the nasal bone on the superior and inferior aspects of the skull. A template  
84 was used to remove arachnoid samples from the left and right sides of the frontal and occipital  
85 regions of the brain. 10 ex-vivo samples were tested with uniaxial tension at  $2 \text{ mm s}^{-1}$ , average  
86 strain rate of  $0.59 \text{ s}^{-1}$ , until failure at <5 hours post extraction. The force and displacement data  
87 were acquired at 100 Hz using LabVIEW. PAC tissue collagen fiber microstructure was  
88 characterized using second-harmonic generation (SHG) imaging on a subset of n=4 stained tissue  
89 samples. To differentiate transverse blood vessels from SAT by visualization of cell nuclei and  
90 endothelial cells, samples were stained with DAPI and anti-von Willebrand Factor, respectively.  
91 The Mooney-Rivlin model for average stress-strain curve fit was used to model PAC material  
92 properties.

93 Results: The elastic modulus, ultimate stress, and ultimate strain were found to be  $7.7 \pm 3.0 \text{ MPa}$ ,  
94  $2.7 \pm 0.76 \text{ MPa}$ , and  $0.60 \pm 0.13$ , respectively. No statistical significance was found across brain

95 dissection locations in terms of biomechanical properties. SHG images were post-processed to  
96 obtain average SAT fiber intersection density, concentration, porosity, tortuosity, segment length,  
97 orientation, radial counts, and diameter as 0.23%, 26.14%, 73.86%,  $1.07\pm 0.28$ ,  $17.33\pm 15.25$   $\mu\text{m}$ ,  
98  $84.66\pm 49.18^\circ$ , 8.15%,  $3.46\pm 1.62$   $\mu\text{m}$ , respectively.

99 Conclusion: For the sizes, strain, and strain rates tested, our results suggest that ovine PAC  
100 mechanical behavior is isotropic, and that the Mooney-Rivlin model is an appropriate curve-fitting  
101 constitutive equation for obtaining material parameters of PAC tissues.

102

## 103 **1.0 INTRODUCTION**

104 The pia-arachnoid complex (PAC), commonly known as the leptomeninges of the brain,  
105 provides mechanical stability for the brain and spinal cord in all vertebrate species [1, 2] The PAC  
106 lies deep to the dura mater and superficial to the brain, and is comprised of the pia mater, arachnoid  
107 mater and the subarachnoid space (SAS). The SAS is filled with cerebrospinal fluid (CSF) and  
108 contains subarachnoid trabeculae (SAT) which span the intermediate area of the meninges (**Fig.**  
109 **1**). SAT are collagen fibers that develop as columns or sheets spanning the SAS, with lateral and  
110 transverse orientations relative to the pia and arachnoid mater [1, 3]. The unique PAC morphology  
111 suggests that one of its potential functions is to protect the brain from traumatic brain injury (TBI)  
112 through energy distribution and absorption [4].

113 Existing studies have identified the significance of the physiological and biomechanical  
114 properties of PAC in central nervous system (CNS) pathologies, such as TBI, spinal canal stenosis,  
115 and Space Flight Associated Neuro-Ocular syndrome (also called SANS), as well as in  
116 applications such as CSF-based drug delivery [4-7]. Neurosurgical dissection of spinal

117 arachnoiditis, or inflammation of the PAC surrounding the spinal cord, is a procedure believed to  
118 reduce CSF flow obstruction by removing SAT fibers [7-12]. Gottschalk et al. found *in-vivo* flow  
119 alterations due to spinal arachnoiditis [13]. The relevance of SAT fibers has also been investigated  
120 in the context of their potential role in CSF drug delivery and solute transport [14-16].  
121 Additionally, Killer et al. showed a potential for increased intraocular pressure caused by SAT  
122 fibers and by extension this could potentially affect astronauts with space flight associated neuro-  
123 ocular syndrome [17]. Taken together, available data implicates the PAC and SAT in CNS  
124 pathologies. Further investigations of the PAC are needed to improve both treatment options and  
125 preventative care.

126         Increased knowledge of PAC biomechanical properties may improve understanding of  
127 CNS pathology following trauma and enhance potential post-trauma treatments. Currently, a  
128 limited understanding of the mechanical behavior of the PAC and SAT hinders the development  
129 of accurate pathophysiological models of the CNS. A common method of modeling mechanical  
130 responses in the cranial cavity during TBI is finite element analysis. In order to increase model  
131 accuracy, biomechanical properties and microanatomy of the PAC need to be quantified. Previous  
132 studies have excluded or used assumed PAC biomechanical properties in computational fluid  
133 dynamic-models to investigate CSF dynamics [14, 15, 18]. SAT fibers have been found to  
134 potentially increase CSF mixing and pressure gradients throughout the CNS [14, 16, 19], and prior  
135 studies have quantified bovine PAC properties under uniaxial tension, traction, and shear [20-22].  
136 However, more data on PAC across species are needed to show inter-species differentiation and  
137 elucidate how PAC biomechanical properties may affect transient stress loading on the brain  
138 during TBI.

139           The objective of the present study was to quantify nonlinear elastic properties under  
140 uniaxial tension and derive the appropriate material parameters of fresh ovine PAC, using the  
141 Mooney-Rivlin curve-fit model. Additionally, we aimed to characterize SAT structure and  
142 orientation through second-harmonic generation (SHG) imaging, with an automated collagen fiber  
143 structural analysis. Results of this study improve the understanding of the structure and  
144 biomechanical function of the PAC across species, which will advance finite element models and  
145 potentially lead to improved understanding and treatment of PAC-related pathologies.

146

## 147 **2.0 METHODS**

### 148 **2.1 PAC Tissue Collection**

149           Ten ovine brains from approximately 1-year-old animals were harvested from USDA  
150 inspected sheep at the University of Idaho Vandal Meats facility. The animals were euthanized  
151 using a captive bolt and immediately exsanguinated and decapitated. The captive bolt was applied  
152 on the forehead, slightly above a line drawn between the eyes. All samples were visually inspected  
153 for brain tissue damage and prepared for brain removal at <10 minutes (min) post-mortem. Brain  
154 samples were extracted within 30 min post-mortem to minimize potential PAC breakdown. To  
155 access the PAC, the lower mandible was removed by making clean proximal cuts through the  
156 mastoid muscle, connective tissues, and temporomandibular joints on either side of the mouth (**Fig.**  
157 **2a**). A strip of skin ~6 cm wide was removed from the medial portion of the skull to expose a clear  
158 strip of bone to split. The skull was then flipped upside down to expose the inferior portion of the  
159 skull. A steel wedge and hammer were used to split through the hard and soft palate of the mouth.  
160 The head was flipped again and split from the nasal bone along the exposed strip of bone to the

161 superior occipital region. The skull was flipped upside down again to split the inferior portion of  
162 the occipital region, and all connective tissue was cut. During this procedure, the skull was  
163 examined to ensure that the PAC tissue remained intact. The skull was then separated carefully on  
164 the medial cut and the brain was removed in its entirety.

165         The brain was kept moist post-harvest with artificial CSF (EcoCyte Bioscience, Austin,  
166 Texas USA) while four samples were removed from the left and right occipital and frontal lobes  
167 (**Fig. 2b**). Each sample was measured with a clear rectangular template measuring 25 mm long, 10  
168 mm wide, and 3 mm thick. A sample thickness of approximately 3 mm was chosen to include the  
169 PAC layer and underlying brain tissue. Extraction locations varied slightly so that each specimen  
170 would contain at least one sulcus or gyrus, and to avoid any obvious physical damage from the  
171 captive bolt traumatic injury site. Samples were visually inspected for tissue damage and either  
172 submerged in artificial CSF for biomechanical testing or fixed in 4% paraformaldehyde overnight  
173 for imaging. Fixed samples were washed 3 times for 5 min each in phosphate buffered saline (PBS)  
174 and stored in PBS at 4 °C and imaged at a later time. Biomechanical tests were performed within  
175 5 hours post-mortem, using samples submerged in artificial CSF immediately following  
176 dissection.

## 177 **2.2 PAC Biomechanical Testing Preparation**

178         Immediately prior to biomechanical testing, individual brain samples were placed in a 49-  
179 mm diameter petri dish with the arachnoid mater facing down and continually moistened with  
180 artificial CSF. Room temperature (22°C) was maintained throughout uniaxial tension tests. Each  
181 sample cut to ~15 mm long x 5 mm wide and placed on a c-shaped template with a 10-mm long  
182 window (**Fig. 3a**). Each end was secured in this c-clamp using cyanoacrylate glue. The soft brain

183 matter was gently teased away using a scalpel and flat-head forceps until the translucent PAC was  
184 isolated. The dissected tissue was visually confirmed to be the PAC using a dissecting microscope,  
185 and tissue integrity was assessed before the sample was considered testable.

186

### 187 **2.3 PAC Thickness Measurement**

188 To avoid potentially damaging testable PAC samples, a separate set of brain samples  
189 (n=10) were used for an average PAC thickness measurement. A caliper (Model 293-340-30  
190 Mitutoyo, Japan), equipped with a ratchet thimble, was used to measure the thickness of each PAC  
191 sample three times to obtain an average sample thickness. The sample was gently placed flat on  
192 the lower caliper clamp. The caliper was slowly tightened until the ratchet thimble turned over and  
193 a visual examination showed the caliper clamps were in full contact of both side of the PAC. The  
194 average PAC thickness was calculated and used for subsequent calculations related to  
195 biomechanical tests.

### 196 **2.4 Uniaxial Tensile Testing**

197 A custom small-scale uniaxial tensile load frame with a 150 g maximum capacity load cell  
198 (Model 31, Honeywell, Columbus, OH) was used to evaluate biomechanical properties of each  
199 PAC sample [23]. PAC samples were mounted and secured into custom soft tissue grips, and the  
200 paper c-clamp frame was cut to ensure that only the PAC tissue was loaded. Once mounted, width  
201 and length of the sample were measured using ImageJ (NIH, Bethesda, MD). PAC samples were  
202 pulled-to-failure in tension at a constant rate of  $2 \text{ mm s}^{-1}$  (**Fig. 3b**) while a LabVIEW program  
203 (National Instruments, Austin TX) recorded force and displacement data at 100 Hz. A total of 22  
204 ovine PAC samples were tested under uniaxial tension from the frontal and occipital lobes.

205 Samples were discarded if they failed at the grip (n=6), a large blood vessel was present within the  
206 sample (n=2), the cross-section was non-uniform (n=1), or the increasing stress-strain curve was  
207 non-monotonic (n=3). All 10 samples included in the analysis failed at the mid-substance and had  
208 a uniform cross-section.

## 209 **2.5 Mooney-Rivlin Curve Fitting and Material Parameter Estimation**

210 The force-displacement data collected from the experiments were analyzed using a custom  
211 MATLAB script (MathWorks, Natick, MA). A Mooney-Rivlin curve fit model (**Eq.1**) for uniaxial  
212 tension was used to fit the obtained average stress-strain curve (**Fig. 4**), with stretch ratio  $\lambda = \varepsilon +$   
213 1. Mooney-Rivlin constants,  $C_{10}, C_{01}, C_{20}$ , were estimated by a nonlinear least-squares fit using  
214 the MATLAB curve fit tool (Vers. R2018B).

215

$$\sigma_{Uniaxial}^{Eng} = 2C_{10} \left( \lambda - \frac{1}{\lambda^2} \right) + 2C_{01} \left( \lambda - \frac{1}{\lambda^3} \right) + 4C_{20} \left( \lambda - \frac{1}{\lambda^2} \right) \left( \lambda^2 + \frac{2}{\lambda} - 3 \right) \quad (\text{Eq.1})$$

216

217 Young's modulus (E) was calculated by tensile stress ( $\sigma$ ) over engineering extensional  
218 strain ( $\varepsilon$ ) over the linear region (**Eq. 2**). Tensile stress ( $\sigma$ ) is the force exerted on the sample F  
219 divided by the cross-sectional area of the sample A. Engineering strain ( $\varepsilon$ ) is the change in sample  
220 length  $\Delta L$  divided by the initial length  $L_0$  of the sample (**Eq. 3**). The strain rate was calculated as  
221 the strain over the time the force was applied. The stretch ratio used was  $\lambda = \varepsilon + 1$ . MATLAB was  
222 used to calculate Young's modulus and ultimate stress and strain were ascertained as the highest  
223 values before PAC rupture.

224 
$$E = \frac{\sigma}{\varepsilon} = \frac{FL_0}{A\Delta L} \quad (\text{Eq. 2})$$

225 
$$\varepsilon = \frac{\Delta L}{L_0} \quad (\text{Eq. 3})$$

## 226 **2.6 Second Harmonic Generation Imaging (SHG) and Immunofluorescence**

227 SHG imaging was used to visualize the collagen fiber microstructure in PAC samples. Images  
228 were taken at 20x magnification and 860 nm excitation wavelength using a confocal/multiphoton  
229 microscope (Fluoview 1000, Olympus, Valley Center, PA) (**Fig. 5a**). To visualize microvascular  
230 structure and cell nuclei, the samples were fixed in 4% paraformaldehyde for 24 h and washed 3x  
231 with PBS + 0.1% Triton X-100 (PBST). The samples were then blocked with 10% bovine serum  
232 albumin in PBST for 1-hour. To stain blood vessels, samples were incubated with anti-von  
233 Willebrand Factor (ab6994, Abcam, Cambridge MA) primary antibody at 1:1000 dilution ratio in  
234 5% bovine serum albumin in PBST on a rocker overnight at 4°C (**Fig. 5b**). Samples were then  
235 washed 3x for 5 minutes in PBST and incubated with anti-goat Alexa Fluoro 488 secondary  
236 antibody (1:2000 dilution ratio) for 1 h at room temperature. Cell nuclei were co-stained with 4,6-  
237 diamidino-2-phenylindole (DAPI) (Invitrogen). Samples were washed 3 times for 5 minutes each  
238 in PBST and imaged with the confocal microscope (**Fig. 5c**).

239 An automated image-based collagen fiber detection method for use with multi-photon  
240 microscopy [24] was used to derive fiber orientation and structure in multiple planes (**Fig. 6**). Slice  
241 thickness for z-direction stacks was chosen to be 2.32  $\mu\text{m}$ . This method quantified fiber  
242 intersection density, concentration, porosity, tortuosity, segment length, orientation, radial counts,  
243 and diameter. These parameters resulted in imaged samples (n=4) having approximately 20 to 50  
244 slices.

## 245 **2.7 Statistical Analysis**

246 Descriptive statistics were obtained for stress-strain parameters resulting from different PAC  
247 locations (occipital and frontal, and left and right hemispheres). To determine if regional  
248 differences existed between tissue sample locations, a two-sample independent t-test with unequal  
249 variance was applied using MATLAB. The parameters tested were Young's Modulus, ultimate  
250 stress, and ultimate strain. Differences were considered significant at p-value < 0.05.

251

## 252 **3.0 RESULTS**

### 253 **3.1 PAC Mechanical Properties**

254 Testing was performed less than five hours post-mortem with an average strain rate of  $0.59$   
255  $\pm 0.12 \text{ s}^{-1}$ . A two-sample independent t-test applied to the occipital and frontal lobes, and left and  
256 right hemispheres showed no statistically significant differences between regions for Young's  
257 modulus, ultimate stress, or ultimate strain ( $p > 0.05$ ) (**Table 1**). Thus, all samples were pooled to  
258 find average length, width, thickness, Young's modulus, ultimate stress, and ultimate strain of  $4.06$   
259  $\pm 0.61 \text{ mm}$ ,  $3.57 \pm 0.90 \text{ mm}$ ,  $70. \pm 30. \mu\text{m}$ ,  $7.7 \pm 3.0 \text{ MPa}$ ,  $2.7 \pm 0.13 \text{ MPa}$ , and  $0.60 \pm 0.14$ ,  
260 respectively. The isotropic material parameters in the Mooney-Rivlin curve fit,  $C_{10}$ ,  $C_{01}$ , and  $C_{20}$   
261 (Eq.1) were calculated to be 1, -1.004 and 0.629 MPa, respectively (SSE = 0.6552,  $R^2 = 0.985$ ),  
262 with 95% confidence bounds.

### 263 **3.2 SHG Imaging**

264 SHG imaging allowed for visualization of collagen microstructure in terms of sheets,  
265 pillars, and blood vessel walls in a subset of PAC samples ( $n=4$ , **Fig. 5a**). Anti-von Willebrand

266 Factor and DAPI staining confirmed the presence of endothelial cells and cell nuclei throughout  
267 the PAC samples (**Fig. 5b** and **C**). This process helped differentiate SAT from transverse blood  
268 vessels. SAT fibers showed straight and crimp-like morphology (**Fig.5a** and **Fig.6**). Using fiber  
269 tracing and analysis software (**Fig. 6**), the average SAT fiber intersection density, concentration,  
270 porosity, tortuosity, segment length, orientation, radial counts, and diameter were found to be  
271 0.23%, 26.14%, 73.86%,  $1.07\pm 0.28$ ,  $17.33\pm 15.25$   $\mu\text{m}$ ,  $84.66\pm 49.18^\circ$ , 8.15%, and  $3.46\pm 1.62$   $\mu\text{m}$ ,  
272 respectively.

## 273 **4.0 DISCUSSION**

274 This study quantified the mechanical properties of the PAC, with the goal of improving  
275 simulations of TBI and other CNS pathologies. The protocol for material testing and the use of the  
276 Mooney-Rivlin model was similar to previously published studies. However, to our knowledge,  
277 this study represents the first biomechanical and morphological quantification of ovine PAC tissue  
278 under uniaxial tension. Methods for brain extraction/dissection and uniaxial tension experiments  
279 were closely followed according to previous studies. Fresh ovine PAC samples (n=10) were kept  
280 on ice and submerged in artificial CSF between dissection and testing locations. Samples were  
281 removed from ice, taken out of their respective containers and kept moist at room temperature, and  
282 tested within 5 hours post-extraction. SHG imaging and fiber analysis of the collagen  
283 microstructure within the PAC indicated an isotropic collagen structure (for example shown by a  
284 wide range of variation in fiber orientation:  $84.66\pm 49.18^\circ$ ). Taken together, these findings provide  
285 normative values for PAC material properties and structure that can be used for modeling and  
286 understanding disease states.

### 287 **4.1 Comparison of Biomechanical Results to Previous Studies**

288 PAC biomechanical properties under uniaxial tension have been found to vary from ~7 to  
289 65 MPa across a range of species and testing protocols (**Table 1** and **Fig. 7**)[22, 25, 26]. In our  
290 study, Young's modulus was found to be at the lower range of those values at  $7.7 \pm 3.0$  MPa. Prior  
291 work using a testing methodology most comparable to our study identified the Young's modulus  
292 of bovine PAC to be 7.52 MPa, at a strain rate of  $0.5 \text{ s}^{-1}$  [22]. Another study in bovine spinal cord  
293 estimated the spinal PAC to be 17 MPa at a strain rate of  $0.05 \text{ s}^{-1}$  [25]. Here, biomechanical  
294 differences across the four tested regions of the brain were found to be similar, with no statistically  
295 significant differences detected in Young's modulus, ultimate stress and strain, or thickness. These  
296 findings are consistent with prior results in bovine models [21, 25].

297 To our knowledge, human PAC biomechanical properties have not been documented, and  
298 therefore a direct comparison with our results is not possible. While studies using human tissues  
299 are limited, the volume fraction in post-mortem human SAT was found to be 5 to 10% greater in  
300 frontal regions of the brain compared to other regions [27]. In principle, these differences in  
301 volume fraction could lead to relatively small regional differences in mechanical properties, but  
302 these relatively small regional differences were not possible to confirm in the present study. Future  
303 work may confirm or deny the relationship between region-dependent SAT volume fraction and  
304 stress-loading during TBI.

305 Ours is also one of the first studies to measure brain PAC directly in "fresh" unfrozen  
306 samples. The measured PAC thickness averaged  $70 \pm 30 \mu\text{m}$  and was measured using a micrometer  
307 with a thimble compression spring. A prior study used a cryostat sliced sample embedded in cow  
308 cheek muscles and an optical microscope to measure average bovine brain PAC thickness as  $23.6$   
309  $\pm 5.8 \mu\text{m}$  [22]. While existing data in brain PAC are limited, prior studies have found spinal PAC  
310 thickness to vary from roughly 10 to  $300 \mu\text{m}$ , depending on the measurement method [21, 25, 26,

311 28]. Using a camera image obtained from the side of the sample, female ovine spinal cord PAC  
312 was found to have a thickness of  $200 \pm 40 \mu\text{m}$  [28]. Finally, the thickness of rabbit spinal cord  
313 PAC has been estimated at  $12 \pm 3 \mu\text{m}$  [26]. Collectively, variations in thickness across studies  
314 likely result from the different methodologies, species, and regions analyzed. These variations  
315 underscore the importance of generating unique PAC material parameters for simulations based  
316 on the location of the simulated trauma.

## 317 **4.2 PAC Material Model**

318 Similar to previous studies investigating CNS tissue biomechanics[29-31] a Mooney-  
319 Rivlin model was applied to estimate material constants that were based on experimentally  
320 generated stress-strain curves. The present study found the Ovine PAC Mooney-Rivlin material  
321 parameters  $C_{10}$ ,  $C_{01}$ , and  $C_{20}$  (**Eq.1**) to be 1, -1.004 and 0.629 MPa, respectively. The parameters  
322  $C_{10}$ ,  $C_{01}$ , and  $C_{20}$  are material constants related to the distortional response of the tissue, which are  
323 determined according to curve-fitting accuracy requirements in this study. However, the  
324 constitutive relationship described by **Eq. 1** is phenomenological. The use of a phenomenological  
325 constitutive relationship has the characteristic that its material constants do not bear a clear  
326 physiological meaning. Jin et al. also used the Mooney-Rivlin model based on Bovine PAC under  
327 uniaxial tension and found constants to be  $C_{31} = 1.3$  (kPa),  $C_{32} = 56$  (kPa),  $C_{41} = 27.5$  (kPa),  $C_{42} =$   
328  $7.9$  (kPa),  $C_{51} = 16.55$  (MPa),  $C_{52}=8.45$  (MPa) [32]. Other studies have used similar methods  
329 regarding the mathematical model for biological tissues [30, 33-35]. The Mooney-Rivlin model  
330 was also chosen since previous research[36] has found the relation between shear stress and shear  
331 strain to be linear for brain tissue. However, this assumption may not be correct for PAC tissue  
332 that is separate from the brain parenchyma. A constituent-based stress-strain relationship could  
333 help account for the main wall constituents and their structural properties[37], as described by the

334 image-based fiber detection method in our study, giving thus a clear physiological meaning to the  
335 constants defining the elastic properties of the tissue.

### 336 **4.3 Structural Morphology**

337 This study utilized a novel method for SAT morphology quantification. SHG imaging with  
338 an 860 nm wavelength was used to visualize and analyze the type I collagen SAT structure. As the  
339 majority of cranial SAT are type I collagen [38], SHG is an effective tool for producing high  
340 fidelity images of the SAT structure. Additionally, using these images, SAT fiber intersection  
341 density, concentration, porosity, tortuosity, segment length, orientation, radial counts, and  
342 diameter were characterized.

343 SAT fiber morphology has traditionally been studied with scanning electron microscopy,  
344 transmission electron microscopy, and brightfield microscopy. Scanning electron microscopy and  
345 transmission electron microscopy showed that the structural morphology of human (post-mortem)  
346 SAT consisted of pillars, columns, sheets, branched fibrils, and other complex structures with fibril  
347 diameters that varied from 0.5-3  $\mu\text{m}$  [3]. Optical coherence tomography was utilized to show that  
348 SAT fiber diameter varies from 19.2-45.5  $\mu\text{m}$  [27]. Fiber diameter in the human (post-mortem)  
349 bulbar subarachnoid space was also found to be between 0.2-1  $\mu\text{m}$  [39]. The present study used  
350 SHG imaging in concert with a program developed by Koch et al [24] and found fiber diameter of  
351 ovine brain PAC to be  $3.5\pm 1.6 \mu\text{m}$ . Fibril diameter variation is likely due to different species or  
352 varied anatomical sampling locations. Few studies have explored the linkage between morphology  
353 and biomechanical properties. Fabris et al., performed atomic force microscopy indentation and  
354 immunofluorescent staining on ex-vivo rat PAC and found significantly different stiffness with  
355 respect to reflecting trabecular density [40]. They also correlated stiffness with increased

356 vascularization and vimentin density. The linkage between the image-based morphological  
357 characteristics and their specific impact on biomechanical properties should be further explored.

358         Biological tissues typically have a non-linear stress-strain behavior, which is characterized  
359 by a toe region at low strains. Collagen tissues have a wavy structure (crimp) that is thought to  
360 produce this behavior due to its unfolding or rotation of fibers parallel to the stretch direction. [41-  
361 43]. Based on the SHG imaging of the collagen structure in the PAC, which was performed at the  
362 zero-stretch state of the tissue, it is possible that the non-linear stress-strain behavior we observed  
363 is a result of a re-orientation of the underlying collagen fiber network along the stretch direction.  
364 Additional studies are needed to determine how stretch affects the collagen fiber orientation and  
365 structural parameters in the subarachnoid space. To further understand possible location variances  
366 in this matrix, histological analysis of the PAC and the collagen crimp structure is needed.

#### 367 **4.4 Relevance of Results to TBI Modeling**

368         In TBI, stress loads on the brain may be dependent on PAC and SAT morphology, similar  
369 to the significant biomechanical changes observed in spinal cord tissue properties when the PAC  
370 is removed [28]. These morphologies may change after multiple sub-concussive or concussive  
371 impacts, altering the impact stress loads on the brain from future head injuries and ultimately  
372 making the subject potentially prone to TBI. The removal or absence of pia has been shown,  
373 through simulations, to have an important effect on pressure distribution in the spine [44, 45]. The  
374 correlation between how TBI affects morphological changes and how those changes impact  
375 biomechanical properties is still largely unknown, but merits further investigation. Accurate  
376 representation of this tissue in simulations of TBI is critical for protective devices to be developed  
377 in high-risk situations such as impact sports. The provided biomechanical and morphological

378 parameter results give information about a new animal model that can be used for finite element  
379 analysis experiments and interspecies comparisons.

#### 380 **4.5 Limitations**

381 Variability across studies may be dependent on extraction and isolation methods [46] since  
382 PAC is sensitive to temperature and moisture content, and known to degrade and change rapidly  
383 post-mortem [28]. The present study employed methods analogous to prior work [22]. To avoid  
384 potential structural alteration with the testable tissue samples, thickness measurements were  
385 averaged from a separate set of samples (n=10).

386 The resting state of the PAC is pre-stressed *in situ* on the brain. When removed from the  
387 surface of the brain, the tissue shrinks in size to a zero-stress condition. Similar to previous studies,  
388 a zero-stress condition was assumed. In the present study, the load frame coordinates were lowered  
389 by 2 mm after the PAC sample was secured in the soft grips to eliminate pre-stress conditions. An  
390 average strain rate of  $0.59 \text{ s}^{-1}$  was applied because this was the maximum strain rate that could be  
391 delivered by our apparatus. Specimen width was found to change by as much as 63% between its  
392 pre-stressed condition situated on the brain, to its unstressed condition in the C-clamp pre-test. To  
393 remain consistent with previous studies, room temperature (22°C) was maintained throughout  
394 uniaxial tension tests [21, 22, 47]. Dehydration was shown to increase stiffness and strength in  
395 tissues made of collagen [48]. Other biological tissues show biomechanical alterations due to  
396 dehydration including the cellular level [49-51] [52]. Anti-drying methods include saline solution  
397 spray [53, 54], silicone adhesive coating [55], silicon oil [56], or submersion in a saline bath [57].  
398 The present study kept the samples hydrated with artificial CSF. Hartmann et al. developed the

399 only known technique for in-vivo human SAT visualization and reported the depths of different  
400 neural structures [58]. This technique could be modified to obtain SAT morphological parameters.

401 In addition to the potential of tissue degradation, this study had a relatively low sample  
402 size. This was due to the number of brains and PAC samples that experienced visible tissue  
403 damage. Future studies may develop a gentler dissection method to protect the tissues.  
404 Additionally, average sample thickness was quantified using samples from multiple areas of the  
405 brain. While tests showed no significant difference in the mechanical properties of the four sample  
406 locations, future studies could control thickness based on the area (occipital, frontal and etcetera).  
407 Finally, this study did not control for age or sex. With higher sample sizes it would be possible to  
408 determine variances that occur with age or sex in addition to location.

409 Importantly, this and many previous studies were carried out using animal tissues. As our  
410 work potentially indicates that mechanical properties of the PAC vary based on species,  
411 quantifying the difference in mechanical properties relative to human tissue is vital for generating  
412 appropriate mechanical parameters for simulations of human TBI. Additional work could be  
413 carried out in concussed and non-concussed human samples of individual SAT fibers. These tests  
414 could be done along multiple axis with multiple strain rates. Future studies could be also be  
415 conducted with an alternative apparatus to test for higher strain rates that would be more applicable  
416 in TBI. An increased sample size could improve statistical significance of stress strain relationship  
417 between brain location and species.

418

## 419 **5.0 CONCLUSION**

420           This study represents the first biomechanical characterization of ovine PAC tissue.  
421 Methods were successfully developed to rapidly harvest and test samples across four extraction  
422 locations. Results are consistent and reproducible with previous studies of PAC biomechanical  
423 properties. This can be used to narrow hypotheses made about the stress-strain curve of PAC across  
424 different species and, in the future, humans. Further development of the understanding of PAC  
425 properties can be used to establish boundary conditions and nonhomogeneous material properties  
426 for numerical modeling of TBI under variable stress loads.

427

#### 428 **LIST OF ABBREVIATIONS**

429	CSF:	Cerebrospinal Fluid
430	CNS:	Central Nervous System
431	DAPI:	4,6-diamidino-2-phenylindole
432	PAC:	Pia-Arachnoid Complex
433	PBS:	Phosphate Buffered Saline
434	PBST:	Phosphate Buffered Saline with Triton
435	SAT:	Subarachnoid Trabeculae
436	SHG:	Second Harmonic Generation
437	TBI	Traumatic Brain Injury

438 **DECLARATIONS**

439 **Ethics approval and consent to participate**

440 This study was approved as exempt by the local governing IACUC review board.

441

442 **Consent for publication**

443 N/A

444

445 **Availability of data and material**

446 The datasets used and/or analyzed during the current study are available from the corresponding  
447 author on reasonable request.

448

449 **Competing interests**

450 BAM is a full-time employee of Alcyone Therapeutics and has received grant support from  
451 Minnetronix Neuro, Biogen, Genentech, Voyager Therapeutics, and Alcyone Therapeutics. BAM  
452 is a scientific advisory board member for Alcyone Lifesciences, International Society for  
453 Hydrocephalus and CSF Disorders, and the Chiari and Syringomyelia Foundation and serves as a  
454 consultant to Flux Neuroscience, Genentech, Roche, Biogen, Praxis Medicines, InviCRO,  
455 SwanBio Therapeutics, Cerebral Therapeutics, Minnetronix Neuro, and CereVasc.

456

457 **Funding**

458 This work was supported by an Institutional Development Award (IDeA) from the National  
459 Institute of General Medical Sciences (NIGMS) of the National Institutes of health (NIH) under  
460 Grant #P20GM1033408 (Martin & Schiele) and #4U54GM104944-04TBD (Martin), NIH  
461 National Institute of Neurological Disorders and Stroke under Grant #R01NS111283, American  
462 Heart Association under Grant [19TPA34860008 to BCWT] (Tanner), and National Science  
463 Foundation under Grant [1656450 to BCWT] (Tanner).

464

465 **Authors' contributions**

466 Study conception and design: BAM, NRS, GKM, GP, MM

467 Acquisition of data: BAM, GCN, GB, GKM, SKT, NRS, CLM

468 Analysis and interpretation of data: BAM, GCN, GB, NRS, SKT, GKM, AT

469 Drafting of manuscript: BAM, GCN, GB, SKT, GKM

470 Critical revision: BAM, MM, BT, NRS, AT, GP

471

472 **Acknowledgements**

473 Goutham Burla<sup>1</sup>

474 Email: gbrula@uidaho.edu

475 Phone: +001 208 885 1030

476

477 Claire L. Majors<sup>1</sup>

478 Email: lucy8500@vandals.uidaho.edu

479 Phone: +001 208 885 1030

480

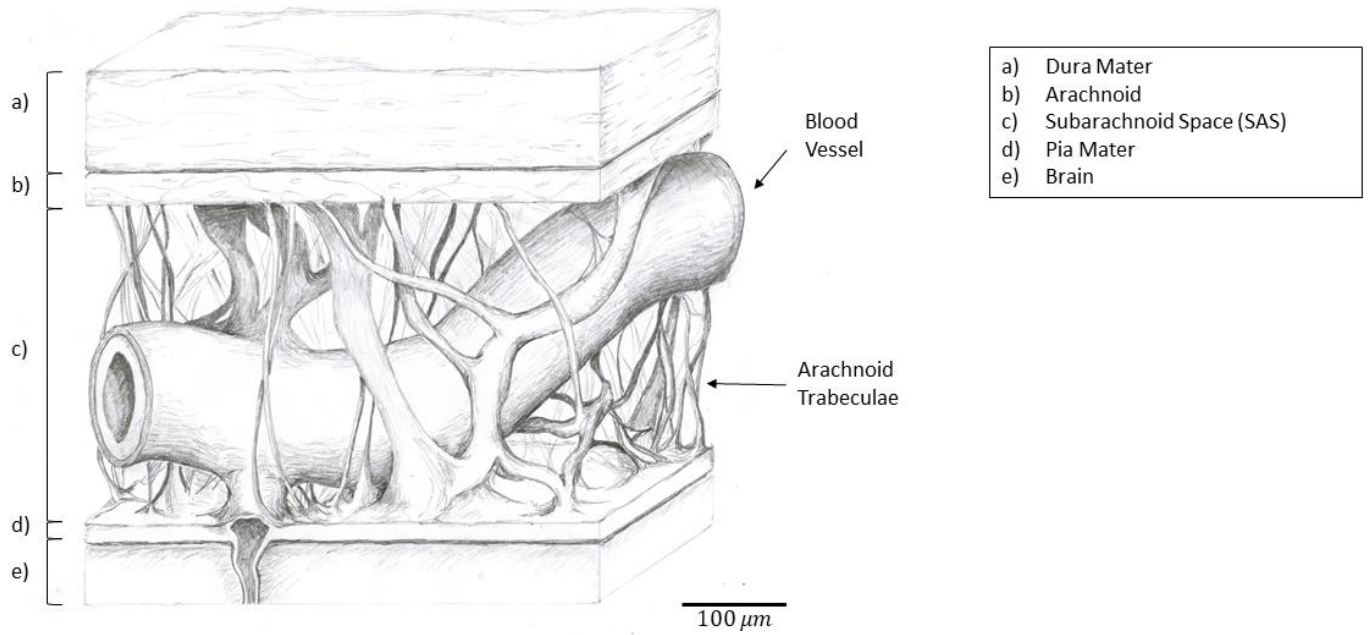
481 James Nasados

482 Email: jnasados@uidaho.edu

483 Phone: +001 208 885 6727

484

485 **FIGURES**



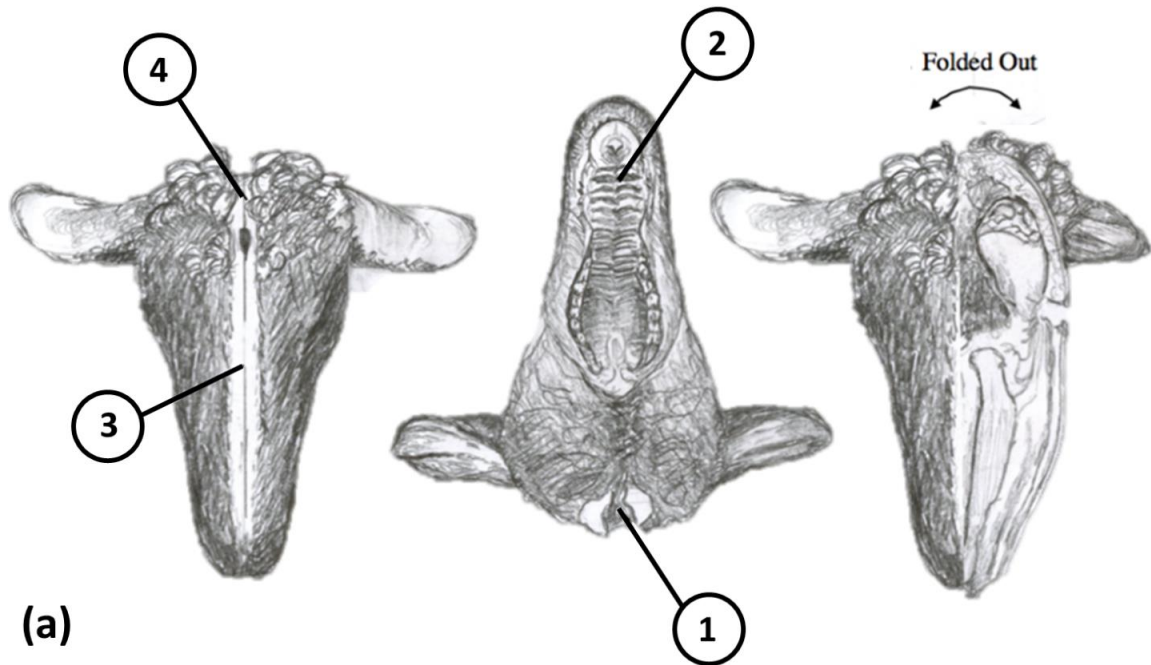
486

487 Figure 1. Anatomical drawing of pia arachnoid complex showing the a) dura mater, b) arachnoid  
488 mater, c) subarachnoid space containing the arachnoid trabeculae fibers and blood vessels, d) pia  
489 mater, and e) brain tissue.

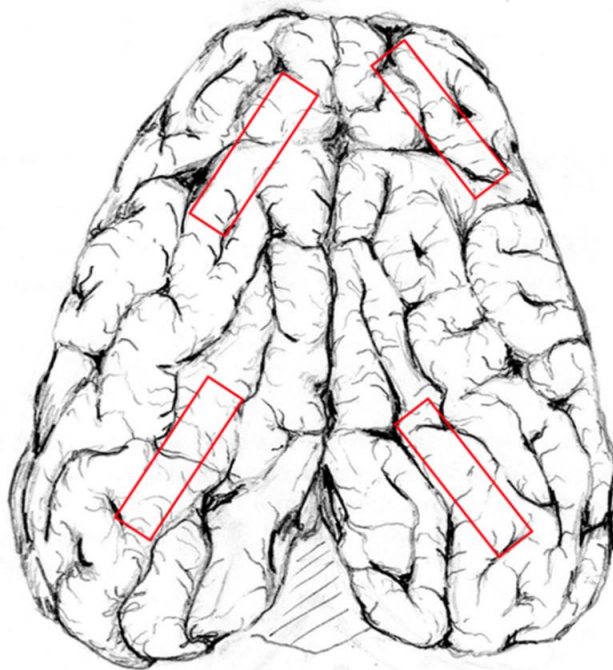
490

491

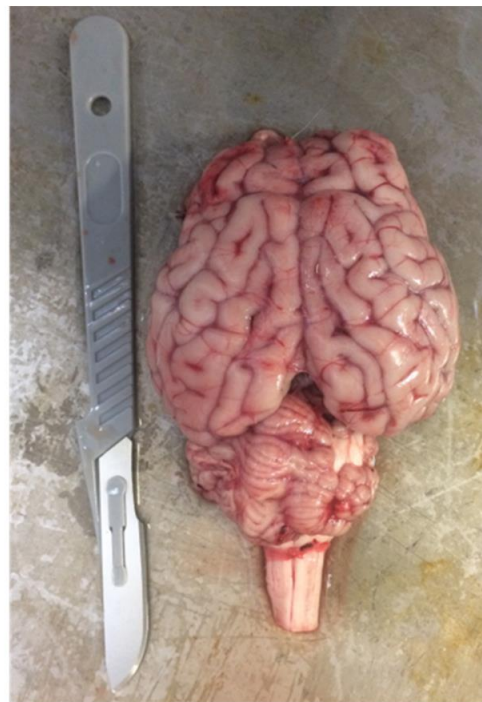
492



(a)



(b)



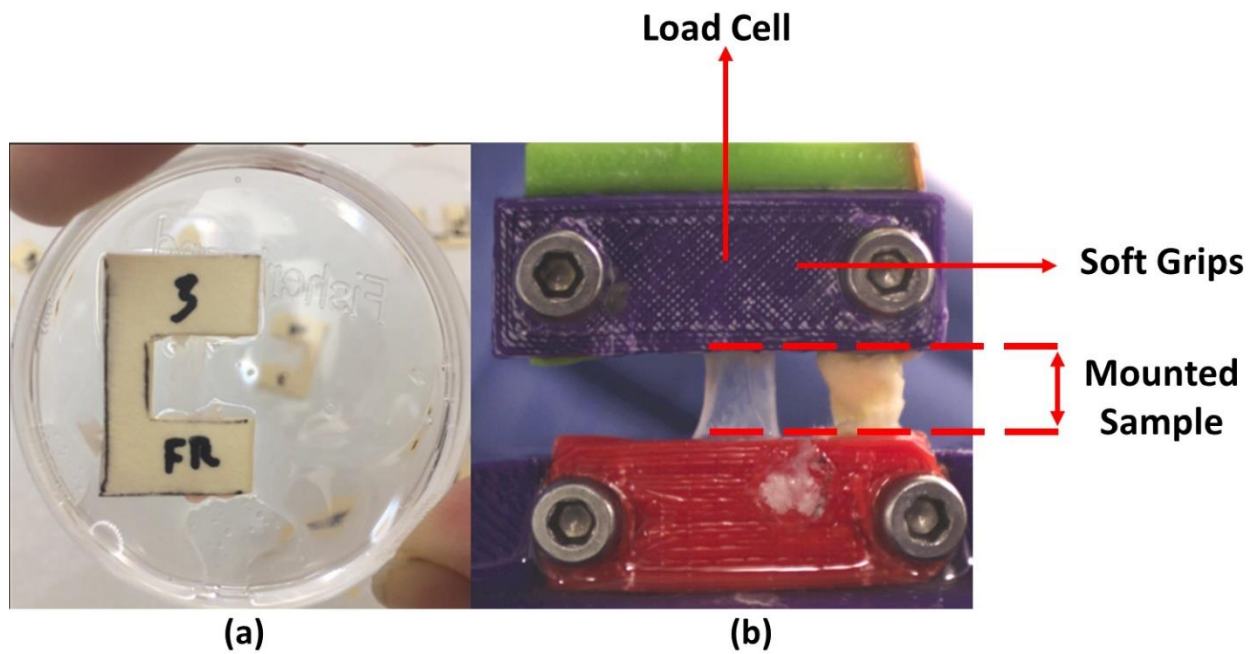
493

494 Figure 2. Procedure for dissection of the ovine PAC tissue. a) Initial midline incision is made on  
 495 superior and inferior aspect of the skull with lower mandible removes. Cuts are made  
 496 sequentially (1-4). b) Location of dissection of occipital and frontal PAC tissue sample removal  
 497 and visual image of dissected ovine brain.

498

499

500



501

502

503

504

505

506

507

508

509

510

511

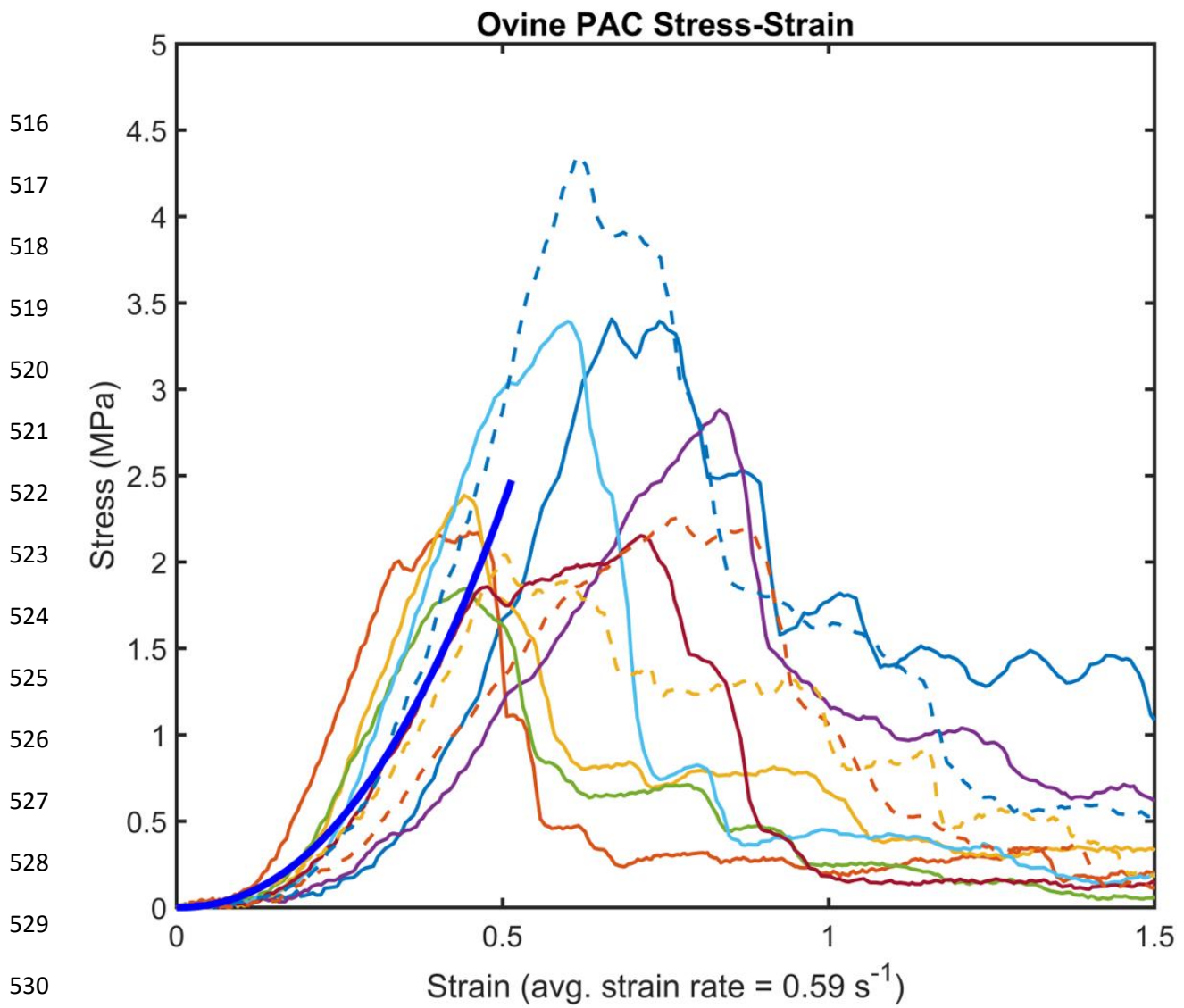
512

513

514

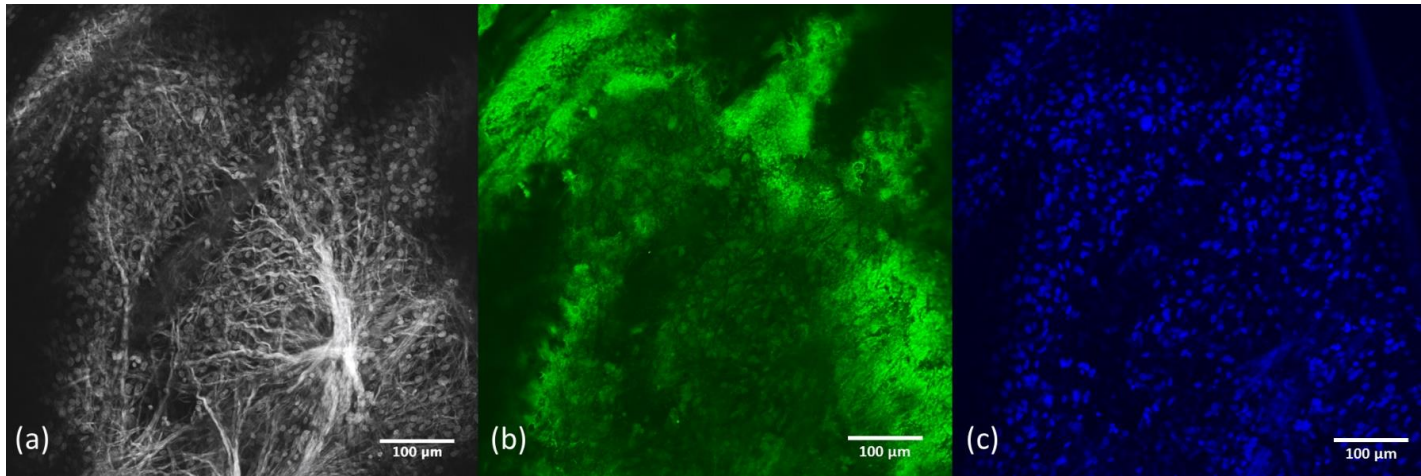
515

Figure 3. (a) PAC with brain matter removed and placed in C-shaped template used for fixture into the load cell. (b) Bioreactor apparatus with mounted sample within grips and orientation of load cell uniaxial tension.



531 Figure 4. Stress-strain curves of the ovine PAC specimens when subjected to uniaxial tension.  
532 Average curve shown in dark blue.

533  
534  
535  
536  
537  
538



539

540 Figure 5. (a) Second Harmonic Generation (SHG) imaging of the PAC at 860 nm. (b) Anti-Von  
541 Willebrand Factor applied at a concentration by volume of 1:1000 to view the membrane lining  
542 of endothelial cells in blood vessels. (c) DAPI applied at concentration by volume of 1:1000 to  
543 view cell nuclei.

544

545

546

547

548

549

550

551

552

553

554

555

556

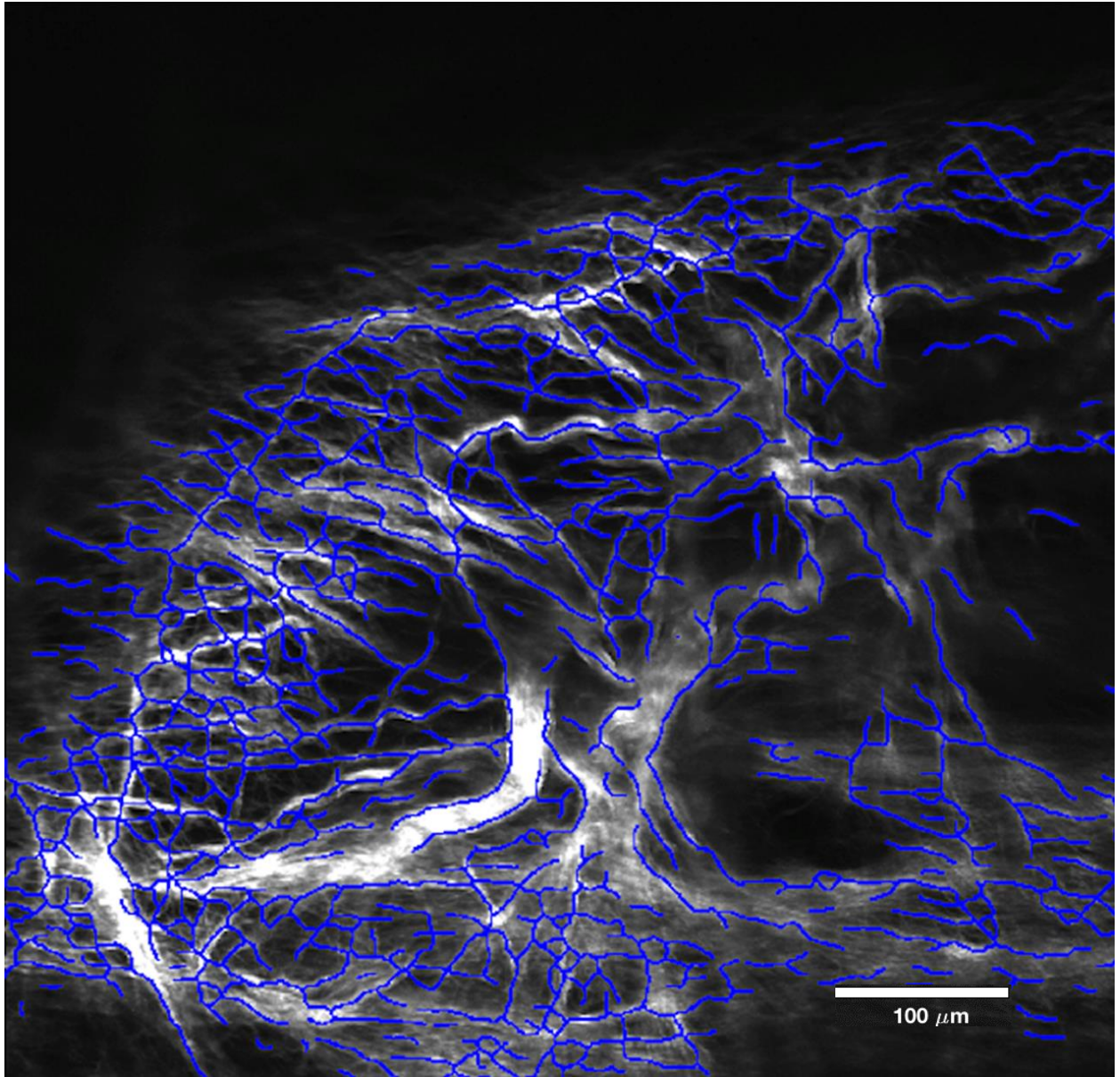
557

558

559

560

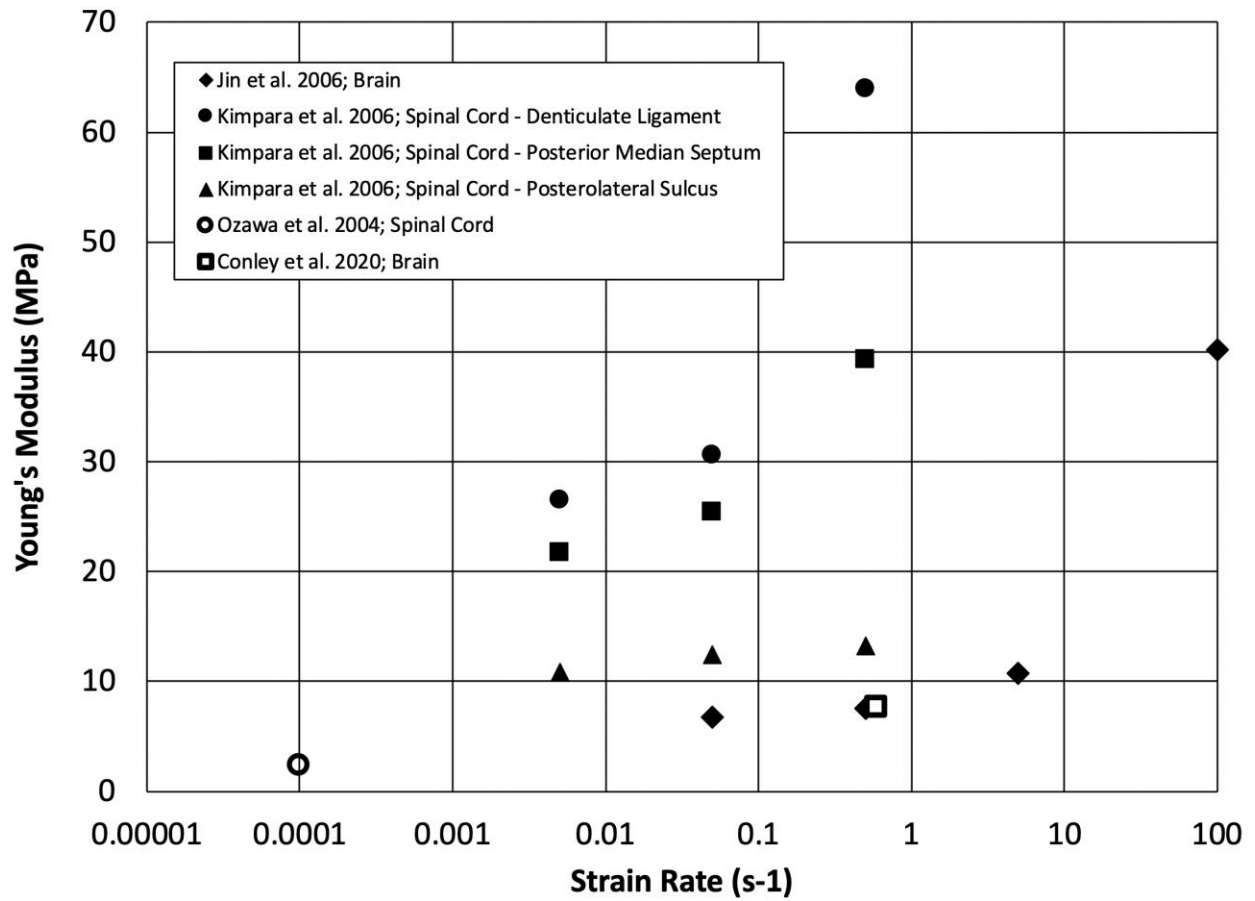
561



562 Figure 6. Single image of the SHG image stack from fiber analysis code developed by Koch et al.  
563 Blue lines depict fiber analysis result (skeleton) used to compute fiber-related parameters (see  
564 methods) [24].

565  
566  
567  
568  
569  
570  
571  
572  
573

574  
575  
576  
577



578  
579  
580  
581  
582  
583  
584  
585  
586  
587  
588  
589  
590  
591  
592  
593

Figure 7. Relation of Young's Modulus and strain rate computed for previous studies published in the literature based on isolated PAC in the spine and brain across bovine, ovine, porcine, and rabbit.

594 **TABLES**

595

596 **Table 1.** Review of previously published literature documenting PAC mechanical properties and  
597 comparison of results to the present study.

598

ref.	Tissue	Species	Young's Modulus (MPa)	Test Method	Strain Rate (s <sup>-1</sup> )	Ult. Stress (MPa)	Ult. Strain (%)	Extraction location
<b>Conley et al. 2020 (Present Study)</b>	PAC	Ovine	7.68 ± 3.0	Tensile	0.59	2.69±0.76	0.60±0.13	Brain
Jin et al., 2006	PAC	Bovine	6.75±0.75	Tensile	0.05	1.05±0.04	35.5±3.9	Brain
Jin et al., 2006	PAC	Bovine	7.52±0.59	Tensile	0.5	1.17±0.13	37.1±2.2	Brain
Jin et al., 2006	PAC	Bovine	10.78±0.58	Tensile	5	1.53±0.11	30.0±3.3	Brain
Jin et al., 2006	PAC	Bovine	40.19±3.54	Tensile	100	3.48±0.25	21.0±1.6	Brain
Kimpara et al., 2006	PAC	Porcine	26.5±3.51	Tensile	0.005	9.8±1.7	43.2±5.6	Spinal Cord - Denticulate ligament
Kimpara et al., 2006	PAC	Porcine	30.6±7.35	Tensile	0.05	10.7±3.1	45.6±12.7	
Kimpara et al., 2006	PAC	Porcine	63.9±13.0	Tensile	0.5	20.1±3.4	37.7±11.0	
Kimpara et al., 2006	PAC	Porcine	21.7±2.88	Tensile	0.005	6.0±1.8	29.2±5.6	Spinal cord - Posterior median septum
Kimpara et al., 2006	PAC	Porcine	25.4±3.61	Tensile	0.05	7.2±1.2	35.0±4.8	
Kimpara et al., 2006	PAC	Porcine	39.3±10.4	Tensile	0.5	9.7±2.5	31.6±6.3	
Kimpara et al., 2006	PAC	Porcine	10.8±1.74	Tensile	0.005	2.1 ± 0.6	23.2±5.5	Spinal Cord - Posterolateral sulcus
Kimpara et al., 2006	PAC	Porcine	12.4±1.13	Tensile	0.05	2.3 ± 0.4	21.6 ± 5.1	
Kimpara et al., 2006	PAC	Porcine	13.2±0.98	Tensile	0.5	2.6 ± 0.6	23.4±6.5	
Ozawa et al., 2004	PAC	Rabbit	2.3	Tensile	N/A	N/A	N/A	Spinal Cord

599

600

601

602

603

604

605 **References**

- 606 [1] M. M. Mortazavi, S. A. Quadri, M. A. Khan, A. Gustin, S. S. Suriya, T. Hassanzadeh, *et al.*,  
607 "Subarachnoid Trabeculae: A Comprehensive Review of Their Embryology, Histology,  
608 Morphology, and Surgical Significance," *World Neurosurg*, vol. 111, pp. 279-290, Mar 2018.
- 609 [2] K. L. Moore and A. F. Dalley, *Clinically oriented anatomy*, 4th ed. Philadelphia: Lippincott  
610 Williams & Wilkins, 1999.
- 611 [3] P. Saboori and A. Sadegh, "Histology and Morphology of the Brain Subarachnoid Trabeculae,"  
612 *Anat Res Int*, vol. 2015, p. 279814, 2015.
- 613 [4] G. G. Scott and B. Coats, "Microstructural Characterization of the Pia-Arachnoid Complex Using  
614 Optical Coherence Tomography," *IEEE Trans Med Imaging*, vol. 34, pp. 1452-1459, Jul 2015.
- 615 [5] S. Margulies, M. Prange, B. S. Myers, M. R. Maltese, S. Ji, X. Ning, *et al.*, "Shaken baby  
616 syndrome: a flawed biomechanical analysis," *Forensic Sci Int*, vol. 164, pp. 278-9; author reply  
617 282-3, Dec 20 2006.
- 618 [6] B. A. Martin and F. Loth, "The influence of coughing on cerebrospinal fluid pressure in an in  
619 vitro syringomyelia model with spinal subarachnoid space stenosis," *Cerebrospinal Fluid Res*,  
620 vol. 6, p. 17, Dec 31 2009.
- 621 [7] C. D. Bertram, L. E. Bilston, and M. A. Stoodley, "Tensile radial stress in the spinal cord related  
622 to arachnoiditis or tethering: a numerical model," *Med Biol Eng Comput*, vol. 46, pp. 701-7, Jul  
623 2008.
- 624 [8] C. L. Davidoff, S. Liu, J. H. Y. Wong, S. Koustais, J. M. Rogers, and M. A. Stoodley, "Treatment  
625 of Syringomyelia in Patients with Arachnoiditis at the Craniocervical Junction," *World*  
626 *Neurosurg*, vol. 107, pp. 565-573, Nov 2017.
- 627 [9] I. Koyanagi, Y. Iwasaki, K. Hida, and K. Houkin, "Clinical features and pathomechanisms of  
628 syringomyelia associated with spinal arachnoiditis," *Surg Neurol*, vol. 63, pp. 350-5; discussion  
629 355-6, Apr 2005.
- 630 [10] S. Cheng, M. A. Stoodley, J. Wong, S. Hemley, D. F. Fletcher, and L. E. Bilston, "The presence  
631 of arachnoiditis affects the characteristics of CSF flow in the spinal subarachnoid space: a  
632 modelling study," *J Biomech*, vol. 45, pp. 1186-91, Apr 30 2012.
- 633 [11] J. Klekamp, G. Iaconetta, U. Batzdorf, and M. Samii, "Syringomyelia associated with foramen  
634 magnum arachnoiditis," *J Neurosurg*, vol. 97, pp. 317-22, Oct 2002.
- 635 [12] L. E. Bilston, D. F. Fletcher, and M. A. Stoodley, "Focal spinal arachnoiditis increases  
636 subarachnoid space pressure: a computational study," *Clin Biomech (Bristol, Avon)*, vol. 21, pp.  
637 579-84, Jul 2006.
- 638 [13] A. Gottschalk, B. Schmitz, U. M. Mauer, A. Bornstedt, S. Steinhoff, B. Danz, *et al.*, "Dynamic  
639 visualization of arachnoid adhesions in a patient with idiopathic syringomyelia using high-  
640 resolution cine magnetic resonance imaging at 3T," *J Magn Reson Imaging*, vol. 32, pp. 218-22,  
641 Jul 2010.
- 642 [14] K. M. Tangen, Y. Hsu, D. C. Zhu, and A. A. Linninger, "CNS wide simulation of flow resistance  
643 and drug transport due to spinal microanatomy," *J Biomech*, vol. 48, pp. 2144-54, Jul 16 2015.
- 644 [15] H. W. Stockman, "Effect of anatomical fine structure on the flow of cerebrospinal fluid in the  
645 spinal subarachnoid space," *J Biomech Eng*, vol. 128, pp. 106-14, Feb 2006.
- 646 [16] H. W. Stockman, "Effect of anatomical fine structure on the dispersion of solutes in the spinal  
647 subarachnoid space," *J Biomech Eng*, vol. 129, pp. 666-75, Oct 2007.
- 648 [17] K. Marshall-Goebel, R. Terlevic, D. A. Gerlach, S. Kuehn, E. Mulder, and J. Rittweger, "Lower  
649 body negative pressure reduces optic nerve sheath diameter during head-down tilt," *J Appl*  
650 *Physiol (1985)*, vol. 123, pp. 1139-1144, Nov 1 2017.
- 651 [18] S. O. Linge, V. Haughton, A. E. Lovgren, K. A. Mardal, and H. P. Langtangen, "CSF flow  
652 dynamics at the craniovertebral junction studied with an idealized model of the subarachnoid  
653 space and computational flow analysis," *AJNR Am J Neuroradiol*, vol. 31, pp. 185-92, Jan 2010.
- 654 [19] S. Gupta, M. Soellinger, D. M. Grzybowski, P. Boesiger, J. Biddiscombe, D. Poulikakos, *et al.*,  
655 "Cerebrospinal fluid dynamics in the human cranial subarachnoid space: an overlooked mediator

656 of cerebral disease. I. Computational model," *J R Soc Interface*, vol. 7, pp. 1195-204, Aug 6  
657 2010.

658 [20] X. Jin, K. H. Yang, and A. I. King, "Mechanical properties of bovine pia-arachnoid complex in  
659 shear," *J Biomech*, vol. 44, pp. 467-74, Feb 3 2011.

660 [21] X. Jin, C. Ma, L. Zhang, K. H. Yang, A. I. King, G. Dong, *et al.*, "Biomechanical response of the  
661 bovine pia-arachnoid complex to normal traction loading at varying strain rates," *Stapp Car  
662 Crash J*, vol. 51, pp. 115-26, Oct 2007.

663 [22] X. Jin, J. B. Lee, L. Y. Leung, L. Zhang, K. H. Yang, and A. I. King, "Biomechanical response of  
664 the bovine pia-arachnoid complex to tensile loading at varying strain-rates," *Stapp Car Crash J*,  
665 vol. 50, pp. 637-49, Nov 2006.

666 [23] A. R. Raveling, S. K. Theodossiou, and N. R. Schiele, "A 3D printed mechanical bioreactor for  
667 investigating mechanobiology and soft tissue mechanics," *MethodsX*, vol. 5, pp. 924-932, 2018.

668 [24] R. G. Koch, A. Tsamis, A. D'Amore, W. R. Wagner, S. C. Watkins, T. G. Gleason, *et al.*, "A  
669 custom image-based analysis tool for quantifying elastin and collagen micro-architecture in the  
670 wall of the human aorta from multi-photon microscopy," *J Biomech*, vol. 47, pp. 935-943, Mar 21  
671 2014.

672 [25] H. Kimpara, Y. Nakahira, M. Iwamoto, K. Miki, K. Ichihara, S. Kawano, *et al.*, "Investigation of  
673 anteroposterior head-neck responses during severe frontal impacts using a brain-spinal cord  
674 complex FE model," *Stapp Car Crash J*, vol. 50, pp. 509-44, Nov 2006.

675 [26] H. Ozawa, T. Matsumoto, T. Ohashi, M. Sato, and S. Kokubun, "Mechanical properties and  
676 function of the spinal pia mater," *J Neurosurg Spine*, vol. 1, pp. 122-7, Jul 2004.

677 [27] N. Benko, E. Luke, Y. Alsanea, and B. Coats, "Spatial distribution of human arachnoid  
678 trabeculae," *J Anat*, Mar 23 2020.

679 [28] N. L. Ramo, K. L. Troyer, and C. M. Puttlitz, "Viscoelasticity of spinal cord and meningeal  
680 tissues," *Acta Biomater*, vol. 75, pp. 253-262, Jul 15 2018.

681 [29] X. Jin, H. Mao, K. H. Yang, and A. I. King, "Constitutive modeling of pia-arachnoid complex,"  
682 *Ann Biomed Eng*, vol. 42, pp. 812-21, Apr 2014.

683 [30] B. Rashid, M. Destrade, and M. D. Gilchrist, "Mechanical characterization of brain tissue in  
684 simple shear at dynamic strain rates," *J Mech Behav Biomed Mater*, vol. 28, pp. 71-85, Dec 2013.

685 [31] M. Hosseini Farid, A. Eslaminejad, M. Ziejewski, and G. Karami, "A Study on the Effects of  
686 Strain Rates on Characteristics of Brain Tissue," in *ASME 2017 International Mechanical  
687 Engineering Congress and Exposition*, 2017.

688 [32] X. Jin, "Biomechanical response and constitutive modeling of bovine pia-arachnoid complex,"  
689 3380487 Ph.D., Wayne State University, Ann Arbor, 2009.

690 [33] G. E. Leclerc, L. Debernard, F. Foucart, L. Robert, K. M. Pelletier, F. Charleux, *et al.*,  
691 "Characterization of a hyper-viscoelastic phantom mimicking biological soft tissue using an  
692 abdominal pneumatic driver with magnetic resonance elastography (MRE)," *J Biomech*, vol. 45,  
693 pp. 952-7, Apr 5 2012.

694 [34] K. K. Mendis, R. L. Stalnaker, and S. H. Advani, "A constitutive relationship for large  
695 deformation finite element modeling of brain tissue," *J Biomech Eng*, vol. 117, pp. 279-85, Aug  
696 1995.

697 [35] T. Hu and J. P. Desai, "Characterization of Soft-Tissue Material Properties: Large Deformation  
698 Analysis," Berlin, Heidelberg, 2004, pp. 28-37.

699 [36] G. Saccomandi and L. Vergori, "Generalised Mooney–Rivlin models for brain tissue: A  
700 theoretical perspective," *International Journal of Non-Linear Mechanics*, vol. 109, pp. 9-14,  
701 2019/03/01/ 2019.

702 [37] A. Tsamis and N. Stergiopoulos, "Arterial remodeling in response to hypertension using a  
703 constituent-based model," *Am J Physiol Heart Circ Physiol*, vol. 293, pp. H3130-9, Nov 2007.

704 [38] D. E. Haines and G. A. Mihailoff. (2018). *Fundamental neuroscience for basic and clinical  
705 applications (Fifth edition. ed.)*. Available:

- 706 [http://SK8ES4MC2L.search.serialssolutions.com/?sid=sersol&SS\\_jc=TC0001882702&title=Fundamental%20neuroscience%20for%20basic%20and%20clinical%20applications](http://SK8ES4MC2L.search.serialssolutions.com/?sid=sersol&SS_jc=TC0001882702&title=Fundamental%20neuroscience%20for%20basic%20and%20clinical%20applications)  
707
- 708 [39] H. E. Killer, H. R. Laeng, J. Flammer, and P. Groscurth, "Architecture of arachnoid trabeculae,  
709 pillars, and septa in the subarachnoid space of the human optic nerve: anatomy and clinical  
710 considerations," *Br J Ophthalmol*, vol. 87, pp. 777-81, Jun 2003.
- 711 [40] G. Fabris, M. S. Z, and M. Kurt, "Micromechanical heterogeneity of the rat pia-arachnoid  
712 complex," *Acta Biomater*, vol. 100, pp. 29-37, Dec 2019.
- 713 [41] H. A. Guerin and D. M. Elliott, "The role of fiber-matrix interactions in a nonlinear fiber-  
714 reinforced strain energy model of tendon," *J Biomech Eng*, vol. 127, pp. 345-50, Apr 2005.
- 715 [42] A. Viidik, C. C. Danielson, and H. Oxlund, "On fundamental and phenomenological models,  
716 structure and mechanical properties of collagen, elastin and glycosaminoglycan complexes,"  
717 *Biorheology*, vol. 19, pp. 437-51, 1982.
- 718 [43] P. Fratzl, K. Misof, I. Zizak, G. Rapp, H. Amenitsch, and S. Bernstorff, "Fibrillar structure and  
719 mechanical properties of collagen," *J Struct Biol*, vol. 122, pp. 119-22, 1998.
- 720 [44] K. H. Stoverud, M. Alnaes, H. P. Langtangen, V. Haughton, and K. A. Mardal, "Poro-elastic  
721 modeling of Syringomyelia - a systematic study of the effects of pia mater, central canal, median  
722 fissure, white and gray matter on pressure wave propagation and fluid movement within the  
723 cervical spinal cord," *Comput Methods Biomech Biomed Engin*, vol. 19, pp. 686-98, 2016.
- 724 [45] N. S. Elliott, "Syrinx fluid transport: modeling pressure-wave-induced flux across the spinal pial  
725 membrane," *J Biomech Eng*, vol. 134, p. 031006, Mar 2012.
- 726 [46] A. Garo, M. Hrapko, J. A. van Dommelen, and G. W. Peters, "Towards a reliable characterisation  
727 of the mechanical behaviour of brain tissue: The effects of post-mortem time and sample  
728 preparation," *Biorheology*, vol. 44, pp. 51-8, 2007.
- 729 [47] P. Aïmeidieu and R. Grebe, "Tensile strength of cranial pia mater: preliminary results," *J*  
730 *Neurosurg*, vol. 100, pp. 111-4, Jan 2004.
- 731 [48] D. F. Betsch and E. Baer, "Structure and mechanical properties of rat tail tendon," *Biorheology*,  
732 vol. 17, pp. 83-94, 1980.
- 733 [49] J. S. Nyman, A. Roy, X. Shen, R. L. Acuna, J. H. Tyler, and X. Wang, "The influence of water  
734 removal on the strength and toughness of cortical bone," *J Biomech*, vol. 39, pp. 931-8, 2006.
- 735 [50] G. M. Thornton, N. G. Shrive, and C. B. Frank, "Altering ligament water content affects ligament  
736 pre-stress and creep behaviour," *J Orthop Res*, vol. 19, pp. 845-51, Sep 2001.
- 737 [51] A. C. Jayasuriya, J. I. Scheinbeim, V. Lubkin, G. Bennett, and P. Kramer, "Piezoelectric and  
738 mechanical properties in bovine cornea," *J Biomed Mater Res A*, vol. 66, pp. 260-5, Aug 1 2003.
- 739 [52] N. H. Mendelson and J. J. Thwaites, "Cell wall mechanical properties as measured with bacterial  
740 thread made from *Bacillus subtilis*," *J Bacteriol*, vol. 171, pp. 1055-62, Feb 1989.
- 741 [53] K. K. Darvish and J. R. Crandall, "Nonlinear viscoelastic effects in oscillatory shear deformation  
742 of brain tissue," *Med Eng Phys*, vol. 23, pp. 633-45, Nov 2001.
- 743 [54] E. G. Takhounts, J. R. Crandall, and K. Darvish, "On the importance of nonlinearity of brain  
744 tissue under large deformations," *Stapp Car Crash J*, vol. 47, pp. 79-92, Oct 2003.
- 745 [55] G. T. Fallenstein, V. D. Hulce, and J. W. Melvin, "Dynamic mechanical properties of human  
746 brain tissue," *J Biomech*, vol. 2, pp. 217-26, Jul 1969.
- 747 [56] F. Shen, T. E. Tay, J. Z. Li, S. Nigen, P. V. Lee, and H. K. Chan, "Modified Bilston nonlinear  
748 viscoelastic model for finite element head injury studies," *J Biomech Eng*, vol. 128, pp. 797-801,  
749 Oct 2006.
- 750 [57] A. Tamura, K. Omori, K. Miki, J. B. Lee, K. H. Yang, and A. I. King, "Mechanical  
751 characterization of porcine abdominal organs," *Stapp Car Crash J*, vol. 46, pp. 55-69, Nov 2002.
- 752 [58] K. Hartmann, K. P. Stein, B. Neyazi, and I. E. Sandalcioglu, "First in vivo visualization of the  
753 human subarachnoid space and brain cortex via optical coherence tomography," *Ther Adv Neurol*  
754 *Disord*, vol. 12, p. 1756286419843040, 2019.

# Figures

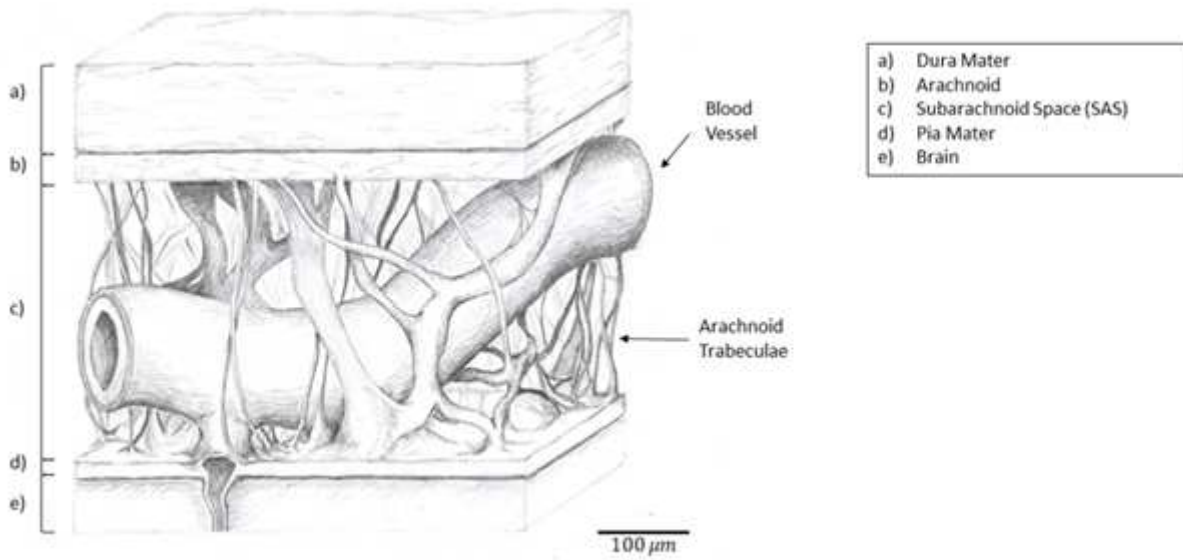
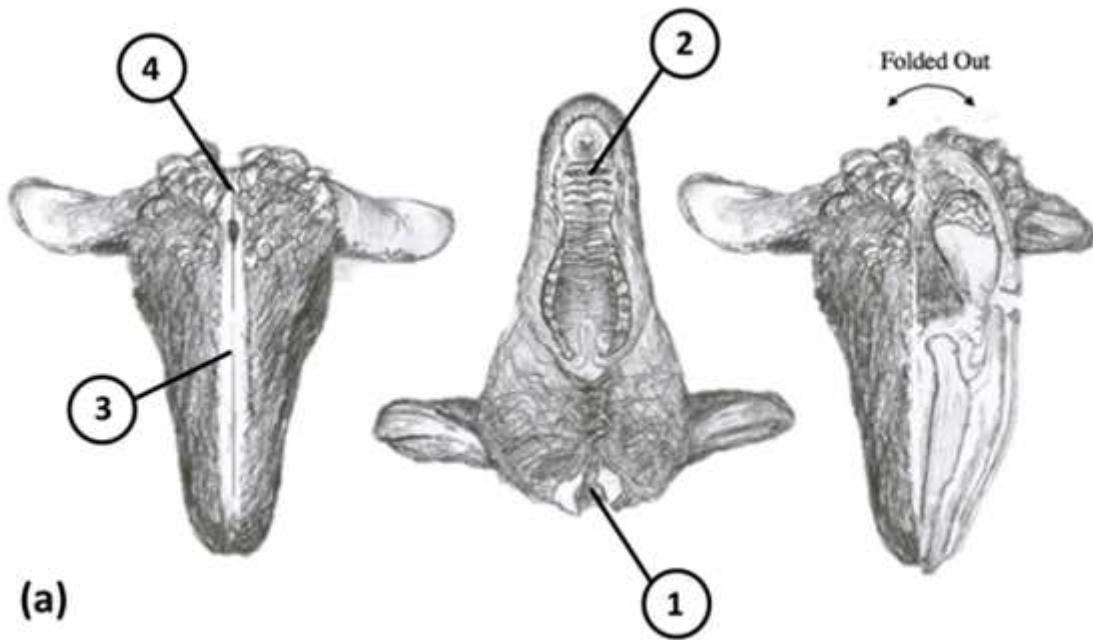
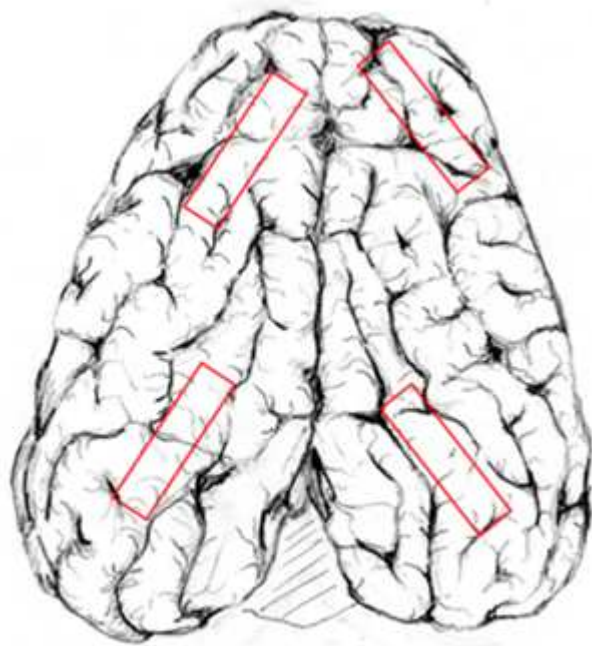


**Figure 1**

Anatomical drawing of pia arachnoid complex showing the a) dura mater, b) arachnoid mater, c) subarachnoid space containing the arachnoid trabeculae fibers and blood vessels, d) pia mater, and e) brain tissue.



(a)



(b)



**Figure 2**

Procedure for dissection of the ovine PAC tissue. a) Initial midline incision is made on superior and inferior aspect of the skull with lower mandible removes. Cuts are made sequentially (1-4). b) Location of dissection of occipital and frontal PAC tissue sample removal and visual image of dissected ovine brain.

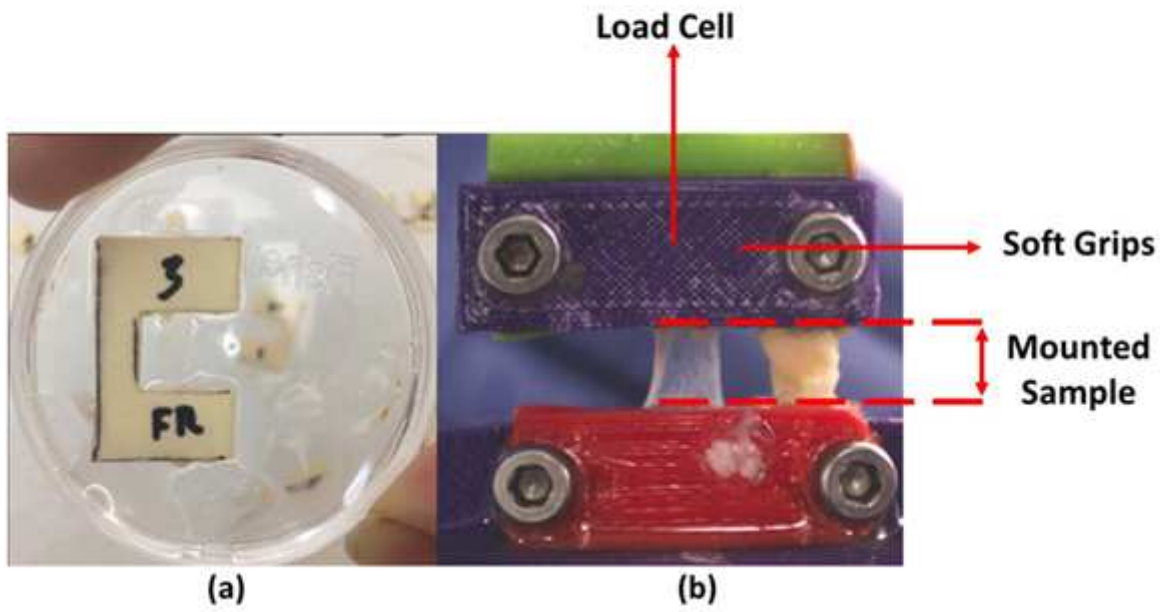


**Figure 3**

(a) PAC with brain matter removed and placed in C-shaped template used for fixture into the load cell. (b) Bioreactor apparatus with mounted sample within grips and orientation of load cell uniaxial tension.

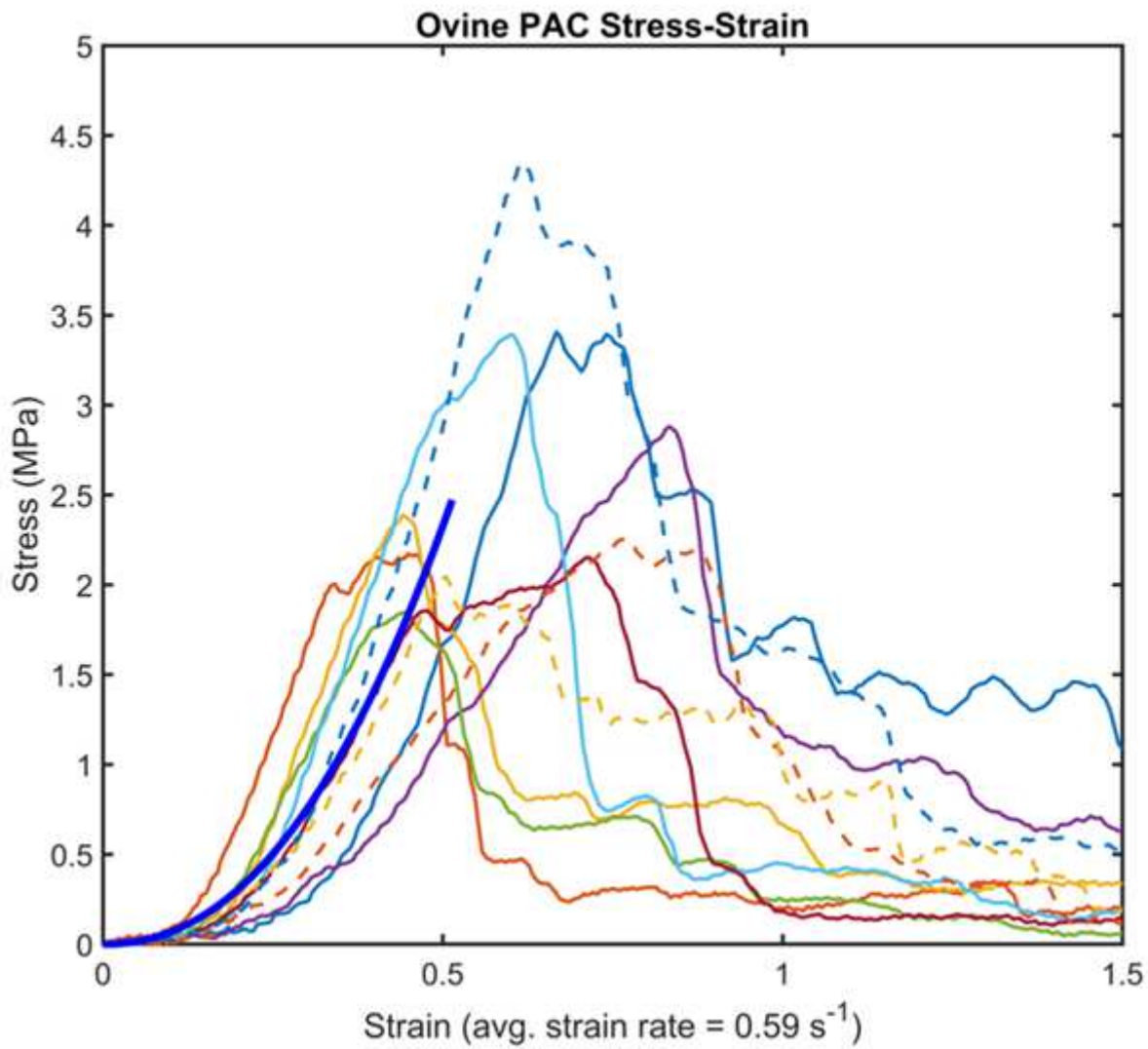


Figure 4

Stress-strain curves of the ovine PAC specimens when subjected to uniaxial tension. Average curve shown in dark blue.

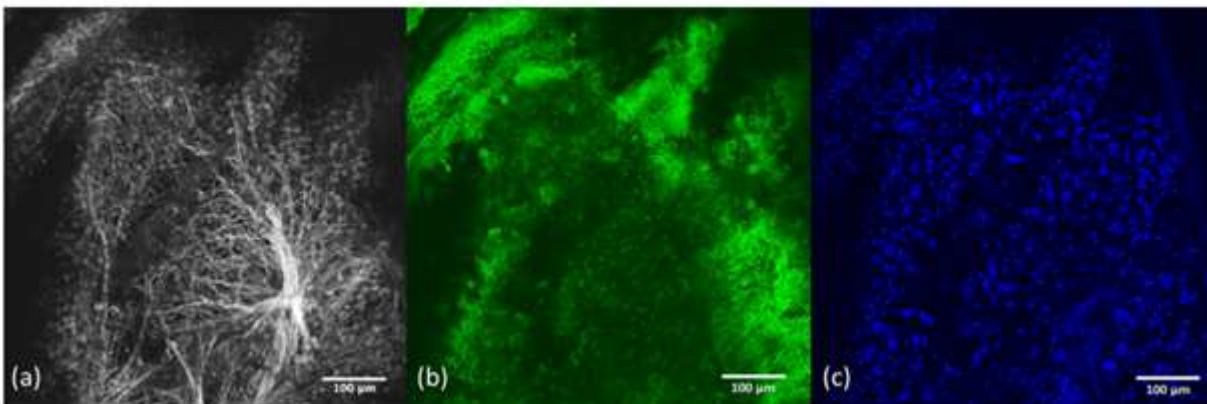
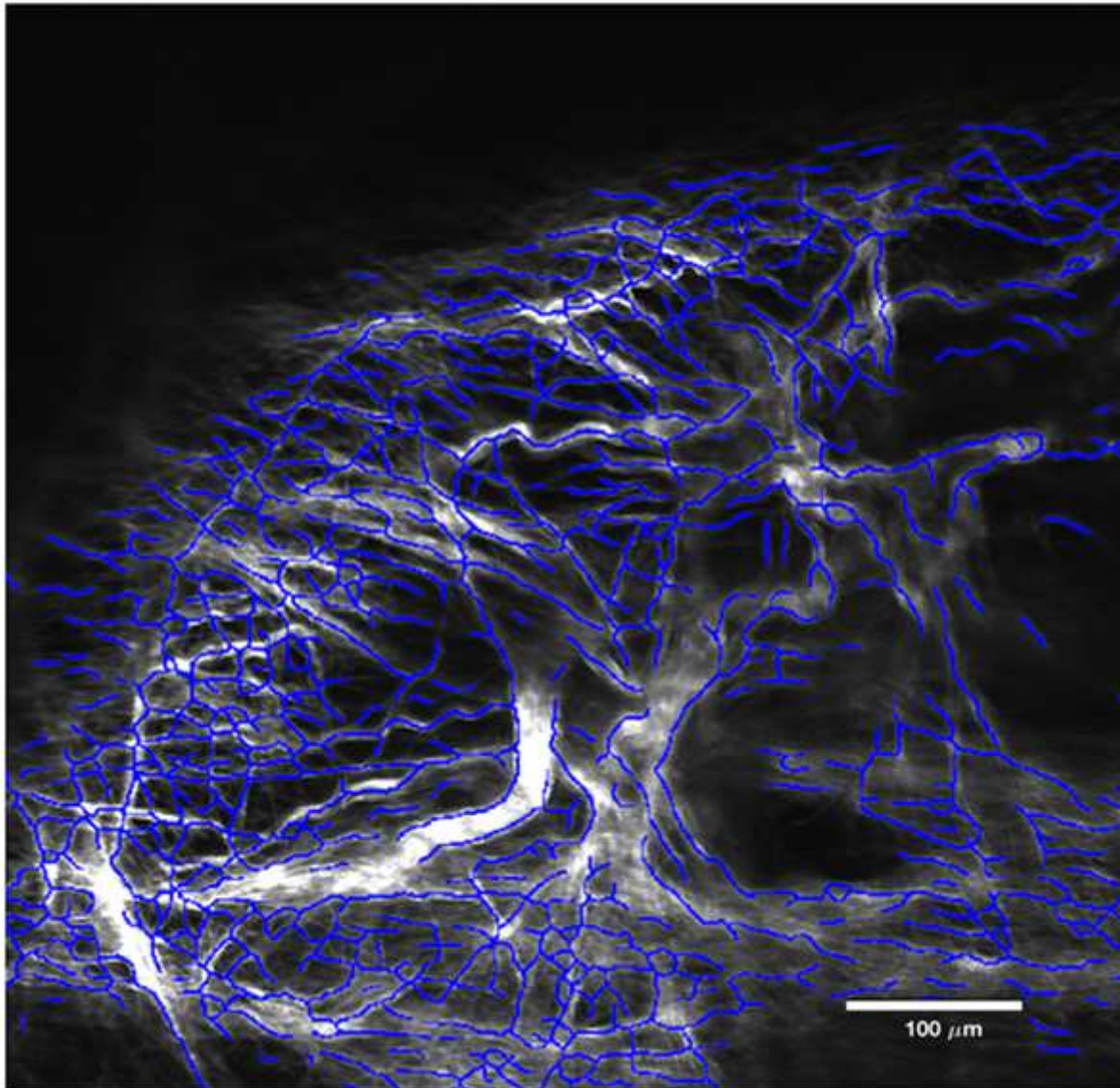


Figure 5

(a) Second Harmonic Generation (SHG) imaging of the PAC at 860 nm. (b) Anti-Von Willebrand Factor applied at a concentration by volume of 1:1000 to view the membrane lining of endothelial cells in blood vessels. (c) DAPI applied at concentration by volume of 1:1000 to view cell nuclei.



**Figure 6**

Single image of the SHG image stack from fiber analysis code developed by Koch et al. Blue lines depict fiber analysis result (skeleton) used to compute fiber-related parameters (see methods) [24].

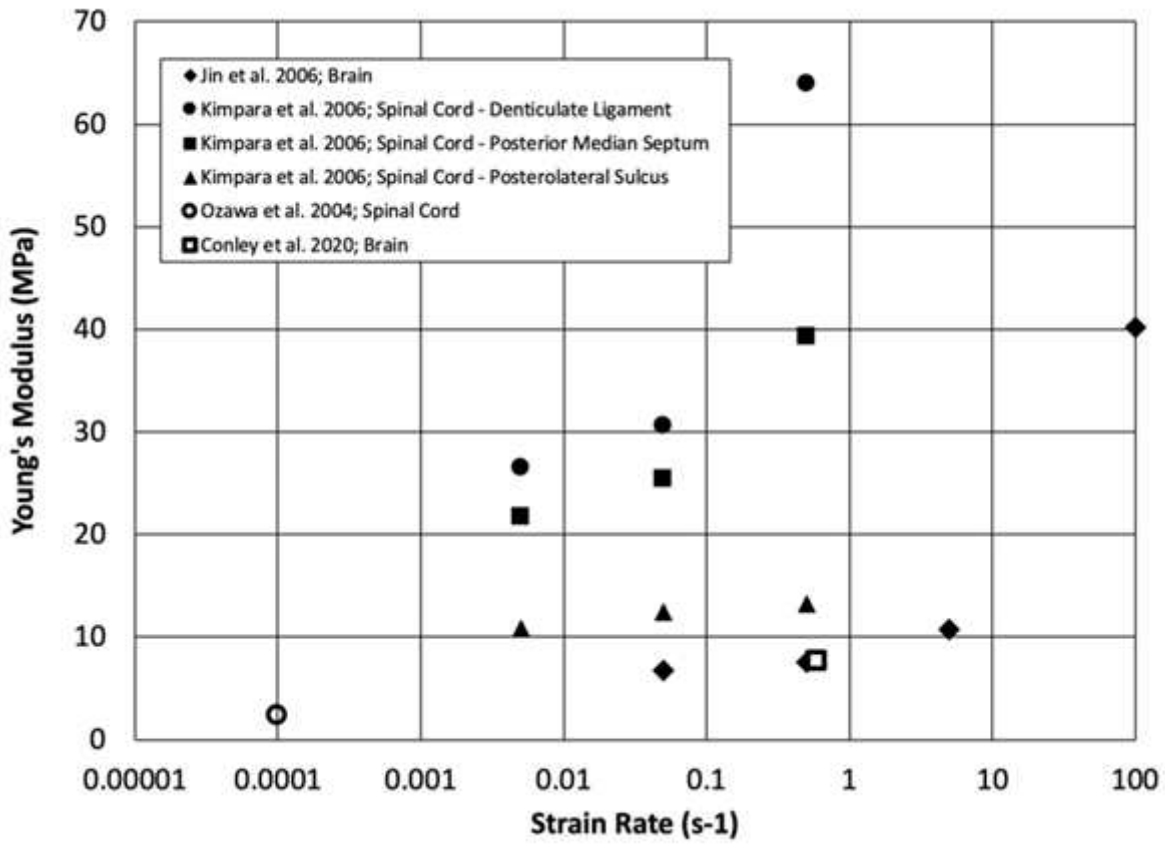


Figure 7

Relation of Young's Modulus and strain rate computed for previous studies published in the literature based on isolated PAC in the spine and brain across bovine, ovine, porcine, and rabbit.